

**Single-ion 4f element magnetism: An *ab-initio* look at
Ln(COT)₂⁻**

Journal:	<i>Dalton Transactions</i>
Manuscript ID	DT-ART-07-2015-002858.R2
Article Type:	Paper
Date Submitted by the Author:	06-Oct-2015
Complete List of Authors:	Gendron, Frédéric; University at Buffalo, State University of New York, Chemistry Pritchard, Benjamin; University at Buffalo, State University of New York, Chemistry Bolvin, Helene; Universite Toulouse, Laboratoire de Chimie Physique Quantique Autschbach, Jochen; University at Buffalo, State University of New York, Chemistry

Single-ion $4f$ element magnetism: An *ab-initio* look at $\text{Ln}(\text{COT})_2^-$

Frédéric Gendron,^a Benjamin Pritchard,^a Hélène Bolvin,^b
and Jochen Autschbach*^a

^a Department of Chemistry, University at Buffalo,
State University of New York, Buffalo, NY 14260-3000, USA

^b Laboratoire de Physique et de Chimie Quantiques,
Université Toulouse 3, 31062 Toulouse, France

email: bolvin@irsamc.ups-tlse.fr, jochena@buffalo.edu

October 6, 2015

Abstract

The electron densities associated with the Ln $4f$ shell, and spin and orbital magnetizations ('magnetic moment densities'), are investigated for the $\text{Ln}(\text{COT})_2^-$ series. The densities are obtained from *ab-initio* calculations including spin-orbit coupling. For Ln = Ce, Pr the magnetizations are also derived from crystal field models and shown to agree with the *ab-initio* results. Analysis of magnetizations from *ab-initio* calculations may be useful in assisting research on single molecule magnets.

1 Introduction

In 1993 it was discovered that a polynuclear metal complex can exhibit 'superparamagnetic-like' properties.¹ Rationalization of the magnetic properties of discrete molecules has since received rapidly growing interest. A single-molecule magnet (SMM) has the ability to retain magnetization for relatively long periods of time. Magnetic relaxation at low temperatures is sufficiently slow to observe magnetic hysteresis, which renders SMMs interesting for molecular spintronics.²⁻⁵ Key features of an SMM are the magnetic anisotropy, and the thermal anisotropy barrier (U_{eff}) between different orientations of the magnetic moment. Due to large intrinsic magnetic moments and often large magnetic anisotropies, lanthanide complexes are of particular interest in the SMM field.^{6,7} For instance, the sandwich complexes $[\text{LnPc}_2]^-$ (Ln^{III} = Tb, Dy, Ho)^{8,9} exhibit a U_{eff} an order of

magnitude higher than transition metal complexes. However, despite strong efforts to characterize and rationalize the SMM behavior of lanthanide systems,^{10–13} their magnetic behavior remains somewhat unpredictable and requires significant theoretical efforts to be rationalized.

To understand the magnetism of a lanthanide complex, detailed knowledge about its electronic structure is crucial. The energy levels within the $4f$ manifold are determined by inter-electron repulsion and the Pauli principle, the spin-orbit (SO) coupling, and the presence of the crystal field (CF). Due to the larger magnitude of the SO coupling compared to the CF interactions in lanthanides, the state ordering is best rationalized by considering first the coupling of the ion's orbital (L) and spin (S) angular momenta at the SO-free (SF) level, and the resulting total angular momentum J upon SO coupling. A multiplet $^{2S+1}L_J$ is then split by the CF. Since the different multiplets are well-separated in energy, typically only the ground state multiplet components $|J, M_J\rangle$ and their mixing under the CF interaction determine the magnetic moment of the ground state.

The magnetic anisotropy of the ground state of lanthanide based molecules can be enhanced by an appropriate combinations of ions and ligand environments.^{14,15} The spatial distribution of the $4f$ electron density has been utilized in the interpretation of the magnetic properties. For this purpose, the angular dependence of the $4f$ charge density of the $|J, M_J\rangle$ states of lanthanide ions has been determined based on models using CF theory.^{14–18} It has been argued that Ln(III) ions having an oblate (equatorially extended) distribution of their $4f$ electron density have larger magnetic anisotropy in an axial environment, whereas equatorial ligands favor larger anisotropy in the case of an prolate (axially extended) $4f$ charge density. The analysis of the angular distribution of the $4f$ charge density of the $|J, M_J\rangle$ states, in combination with parameters of the CF theory, constitutes a simple method to rationalize an environment that will generate a ground state with a large magnetic anisotropy.^{14,15,19}

However, electron density does not in itself contain information about the magnetic moments, and therefore its distribution is not necessarily representative of the magnetic moments and their orbital and spin contributions. Indeed, Boucherle *et al.*²⁰ have shown that the 'shape' of electron and spin densities differ within the Ln(III) series. The 'shapes', meaning here the spatial distributions of the electron and spin densities, are similar for the light rare-earths and opposite for the heavy rare-earths, suggesting that the spin density reflects the electron density in the first-half of the series, whereas it represents the unpaired electrons in the second-half of the series.²¹ Furthermore, as the orbital angular momentum L generally differs from zero in f -element compounds, an important orbital contribution to the magnetic moment appears. Its spatial distribution may differ drastically from the spin density and the electron density. Since the electron density is only indirectly related to the magnetic properties, via the underlying wave function, we aim to explore the various contributions to the magnetic moment with the help of *ab-initio* calculations, with-

out resorting to CF models. However, CF models are used to show that for simple cases CF and *ab-initio* theory give comparable results.

This work aims to highlight the utility of theoretical calculations for the investigation of the magnetic properties of *f*-element complexes. New computational tools were recently developed in our group to generate the 4*f* electron densities as well as the orbital and spin magnetizations from *ab-initio* wavefunctions at the SO level. These tools allow to make a direct comparison with the 4*f* charge density distributions derived previously from CF theory for Ln(III) ions. We aim to demonstrate that such *ab-initio* calculations and accompanying visualizations can be very useful for the rationalization of the magnetic behavior of *f*-element complexes.

To introduce the concept of analyzing the orbital and spin magnetization, and related orbitals, for the study of magnetic complexes, in addition to the established ‘prolate vs. oblate shape’ description of the electron density, we have chosen a systematic series of Ln(III) complexes, namely $\text{Ln}(\text{COT})_2^-$ (COT = cyclooctatetrane). The choice of these complexes is motivated by their electronic ground states, which are comparatively well understood^{22,23} but at the same time – for the most part – out of the reach of single-reference approaches such as Hartree-Fock and Kohn-Sham and in need of treating the SO interaction explicitly. These anionic systems have a structure with D_{8h} symmetry, where the Ln(III) ions are sandwiched by two planar and parallel unsaturated aromatic COT^{2-} ligands in an eclipsed orientation.^{24–26} The $\text{Ln}(\text{COT})_2^-$ complexes have no pronounced 4*f* bonding,²⁷ which allows for a comparison of the *ab-initio* calculations with CF models. (The nature of the ground states of the corresponding neutral complexes and the involvement of the 4*f* shell in the bonding has long been a subject of debate.^{28–32}) The high degree of symmetry imposed by the COT ligands is another reason for choosing the $\text{Ln}(\text{COT})_2^-$ series in the context of SMMs³³ and the present study. Due to the almost perfect axial symmetry, the mixing between the M_J sublevels is limited, reducing the undesired effects in the magnetic relaxation path such as the quantum tunneling of magnetization.³⁴ Therefore, such high symmetrical complexes might favor systems with high M_J ground states and relatively large energy barriers, leading to slow spin relaxation.³⁵ Such SMM behavior was experimentally characterized by the groups of Long and Murugesu for $\text{Er}(\text{COT})_2^-$ ^{34,36–38} and $\text{Dy}(\text{COT})_2^-$,^{37,39} and to a lesser extent for a derivative of the $\text{Ce}(\text{COT})_2^-$ complex.⁴⁰

The strategy as well as the computational and theoretical details used for the calculations of the magnetic properties of the ground state of the entire $\text{Ln}(\text{COT})_2^-$ series are provided in Section 2. The results for $\text{Ce}(\text{COT})_2^-$ and $\text{Pr}(\text{COT})_2^-$ are first discussed in details in Section 3 to illustrate how CF model wavefunctions are used herein to obtain the orbital and spin magnetization, and how these models connect to the *ab-initio* calculations. The magnetization data for the rest of the series are analysed and discussed in Section 4, starting with the assignments of the ground state, analysis of the electron density of the ground states in term of natural orbitals, analysis of the spin

magnetizations in term of natural spin orbitals, and comparisons of calculated vs. experimental magnetic susceptibility χT for selected complexes. Concluding remarks and an outlook can be found in Section 5.

2 Theoretical and computational details

The magnetic moment m_u associated with an electronic doublet and a principal magnetic axis $u \in \{x, y, z\}$ of a complex, is the expectation value of the corresponding operator $\hat{\mu}_u$, given by

$$\hat{\mu}_u = -\mu_B \hat{m}_u = -\mu_B (\hat{L}_u + g_e \hat{S}_u) \quad (1)$$

Here, \hat{L}_u and \hat{S}_u are components of the dimensionless vector operators for the orbital and spin angular momentum, respectively, \hat{m}_u is their combination generating the magnetic moment (dimensionless), μ_B is the Bohr magneton, and $g_e \simeq 2$ is the free electron g -factor. Relativistic corrections to the magnetic moment operator are neglected. Components of the spin ($m_u^S(\mathbf{r})$) and orbital ($m_u^L(\mathbf{r})$) magnetization can be defined accordingly as

$$m_u^L(\mathbf{r}) = \int \psi^\dagger \hat{L}_u \psi d\tau' \quad (2a)$$

$$m_u^S(\mathbf{r}) = g_e \int \psi^\dagger \hat{S}_u \psi d\tau' \quad (2b)$$

Here, the wave function ψ is a linear combination of the components of the multiplet of interest that diagonalizes the $\hat{\mu}_u$ operator. Further, $d\tau'$ implies integration over all but one electron coordinate, and $\psi^\dagger \cdots \psi$ implies ‘integration’ over all spin degrees of freedom. The total magnetic moment μ is then given by simple 3-dimensional volume integrals of the magnetizations:

$$\langle \mu_u \rangle = -\mu_B \int [m_u^L(\mathbf{r}) + m_u^S(\mathbf{r})] dV \quad (3)$$

We use $g_e = 2$. In the absence of SO coupling, m_z^S corresponds to the usual spin density. The spin magnetization components and the electron density (the electron number density, to be precise) are represented by real symmetric matrices in an atomic orbital (AO) basis. These matrices can be diagonalized to give different sets of molecular orbitals. For instance, the electron density $\rho(\mathbf{r})$ is represented by a set of natural orbitals φ_p (NOs) with populations (occupations) n_p that add up to the total number of electrons:

$$\rho(\mathbf{r}) = \sum_p n_p [\varphi_p(\mathbf{r})]^2 \quad \text{with} \quad \sum_p n_p = N \quad (4)$$

In a similar fashion, one obtains from the AO matrices representing the m_u^S sets of natural orbitals for the spin magnetization ('natural spin orbitals', or NSOs) whose spin populations add up to $2\langle S_u \rangle$:

$$m_u^S(\mathbf{r}) = \sum_p n_p^u [\varphi_p^u(\mathbf{r})]^2 \quad \text{with} \quad \sum_p n_p^u = 2\langle S_u \rangle \quad (5)$$

For further details, see Reference 41. In the present work we present NOs and NSO data for m_z^S . All magnetic property calculations were carried out based on complete active space (CAS) self-consistent field (SCF) multi-reference wavefunctions determined as described below. It is important to keep in mind that due to the multi-determinant character of most of the wavefunctions the population numbers are not necessarily integers or half-integers. The NO populations are between 0 and 2. The NSO spin populations are between -1 and 1 , where a 0 either means that the corresponding NO is not occupied or that its population is spin-compensated. Sets of orbitals can also be constructed in relation to the orbital magnetization m_u^L , but their interpretation is somewhat less straightforward and left to a subsequent study.

The magnetizations and the electron densities associated with the $4f$ orbitals were calculated and visualized based on complete active space *ab-initio* wavefunctions as described below and in References 41 and 42. Corresponding spin and orbital angular momentum expectation values and g -factors are also provided in Section 4. Additional data, including plots of NOs and NSOs, can be found in the Supplementary Information (SI).

In the case of $\text{Ln}(\text{COT})_2^-$, idealized geometries have D_{8h} symmetry. The 8-fold axis which connects the COT centroids corresponds to the magnetic axis z and is referred here as the \parallel direction. In this symmetry, the CF Hamiltonian reads in commonly used notation⁴³

$$\hat{H}^{CF} = \beta_J(2)[B_2^0 \tilde{O}_2^0] + \beta_J(4)[B_4^0 \tilde{O}_4^0] + \beta_J(6)[B_6^0 \tilde{O}_6^0] \quad (6)$$

The states are characterized by either integer or half-integer M_J , as shown in the SI, where $M_J = \langle m_{\parallel} \rangle$.

In the following, we use the notation for linear molecules to designate the irreducible representations ('irreps') of the complexes. Except for the case of $M_J = 0$, which is non-magnetic, all other states are doublets with $\pm M_J$ components. For a given direction u , a linear combination of the doublet components diagonalizing $\hat{\mu}_u$ was generated. For consistency, the M_J component with positive $\langle S_u \rangle$ was then used for each system to generate the magnetizations. The component with opposite M_J affords $\langle S_u \rangle, \langle L_u \rangle, \langle m_u \rangle$ of opposite sign. The reason for this choice is that in the absence of orbital angular momentum and SO coupling the state components correspond to electron spin-up and spin-down, respectively.

For comparison with previous studies, an ‘angular dependence function’ $R(\theta)$ of the $4f$ electron number density has been calculated according to Reference 15 with

$$R(\theta) = \sqrt[3]{\tilde{c}_0 + c_2 Y_2^0(\theta) + c_4 Y_4^0(\theta) + c_6 Y_6^0(\theta)} \quad (7)$$

Here, $Y_\ell^m(\theta)$ is a spherical harmonic. The c_ℓ parameters represent the 2^ℓ -multipole moments of the $4f$ electron density and were taken from Reference 15. The monopole term $\tilde{c}_0 = 3/4\pi$ was used in Reference 15 in order to accentuate the apshericity of the densities, as it was also done later in Reference 14. In the present work the $R(\theta)$ functions are compared to the *ab-initio* $4f$ -electron ($\rho^{4f}(\mathbf{r})$) and $4f$ -‘hole’ ($\rho^{\text{hole}}(\mathbf{r})$) densities. These densities were calculated as follows:

$$\rho^{4f}(\mathbf{r}) = \sum_{i \in 4f} n_i [\varphi_i(\mathbf{r})]^2 \quad ; \quad \rho^{\text{hole}}(\mathbf{r}) = \sum_{i \in 4f} (2 - n_i) [\varphi_i(\mathbf{r})]^2 \quad (8)$$

The $\varphi_i(\mathbf{r})$ are the aforementioned NOs representing the $4f$ shell and the n_i are the occupation numbers.

Structures optimizations of the $\text{Ln}(\text{COT})_2^-$ complexes were performed using the 2013 release of the Amsterdam Density Functional (ADF) package.^{44–46} The optimizations utilized the scalar relativistic all-electron zeroth-order regular approximation (ZORA) Hamiltonian,⁴⁷ the B3LYP⁴⁸ hybrid functional, and a triple- ζ doubly polarized all-electron Slater type basis (TZ2P) for ZORA calculations as provided in the ADF basis set library. The structures were optimized in the D_{8h} symmetry point group. The open metal shells were treated with fractional orbital occupations resembling an ‘average of configurations’ (AOC),⁴⁹ where necessary. The main calculated distances are resumed in Table S1 of the SI. Due to the fractional occupation scheme used for the optimizations, frequency calculations could not be performed on most of the complexes of the series. Nevertheless, a numerical frequency analysis was performed on the optimized structure of $\text{Gd}(\text{COT})_2^-$, which confirmed it to be a minimum. A limited influence on the magnetic properties is expected for small geometrical changes in these structures. Recently, Ungur *et al.* showed that the magnetic properties of the ground state and of the first excited states of $\text{Er}(\text{COT})_2^-$ are very similar for a large range of Er-COT distances.³⁷ We performed a similar scan for $\text{Ce}(\text{COT})_2^-$. As shown in Table S2, the lowest SF and SO states in $\text{Ce}(\text{COT})_2^-$ are hardly affected by moderate changes of the Ce-COT distances. Moreover, the low-energy part of the electronic spectra of $\text{Ln}(\text{COT})_2^-$ complexes were found almost independent of the relative orientation of the two COT rings, and therefore can be safely assumed as parallel to each other.³⁷ CASSCF wavefunction calculations were carried out with a developer’s version of Molcas 7.9⁵⁰ using the protocol detailed in References 41, 51. The second-order Douglas-Kroll-Hess scalar relativistic Hamiltonian⁵² was employed in the calculations without SO coupling. All electron ANO-RCC Gaussian-type basis

sets contracted to TZP quality were employed. SO coupling was treated by state interactions between the CASSCF wave functions, using the Restricted Active Space State Interaction (RASSI) program.⁵³ The active space used for the $\text{Ln}(\text{COT})_2^-$ series was $\text{CAS}(n,7)$ which corresponds to the n unpaired electrons in the seven $4f$ orbitals. Due to the small amount of covalency in the lanthanide-ligand bonds, minimal active spaces including only the $4f$ orbitals and $4f$ electrons are sufficient to describe the magnetic properties of lanthanide based complexes.⁷ Furthermore, it has been shown that the use of larger triple- ζ basis sets, as well as the introduction of the doubly occupied $4d$ shell in the active space do not significantly improve the calculations.⁵⁴ The electronic g -factors were calculated according to Reference 55 and the magnetic susceptibilities were calculated using the Single Aniso routine of Molcas as detailed in Reference 56. A local modification^{41,42} of Molcas was used to generate the set of natural orbitals (NOs), natural spin orbitals (NSOs), orbital (m_u^L) and spin (m_u^S) magnetizations. The graphical visualizations of the *ab-initio* orbitals and magnetizations were created with the graphical user interface of the ADF suite.

3 Models for $\text{Ce}(\text{COT})_2^-$ and $\text{Pr}(\text{COT})_2^-$

The cases of the $\text{Ce}(\text{COT})_2^-$ and $\text{Pr}(\text{COT})_2^-$ complexes are discussed first in some detail to illustrate how the orbital and spin magnetizations can be interpreted and how they are related to the CF models and to the *ab-initio* wavefunctions and densities. The $4f$ orbitals are labeled as σ , π , δ , ϕ , referring to the \parallel axis of rotation, and correspond to linear combinations of spherical harmonics with $|m_\ell| = 0, 1, 2, 3$, respectively (see SI). Expressions of the orbital and spin magnetizations in Table 1 are given by linear combination of simple orbital densities. For a many-electron system they are therefore much easier to interpret than the wave function.

In the Ce^{3+} free ion, the ground spectroscopic term $^2F_{5/2}$ is split by the CF into three Kramers doublets. In $\text{Ce}(\text{COT})_2^-$, the $M_J = \pm 1/2$ doublet is the lowest; it derives from the mixing between $^2\Sigma$ and $^2\Pi$ SF states as given in Table 1. The wave function ψ for the ground state (GS) corresponds to an admixture of f_σ and f_π orbitals with opposite spin due to the SO interaction. The real coefficients A and B quantify their contribution to the SO ground state. From *ab-initio* calculations, we obtained $A = 0.74$ and $B = 0.68$, and must be compared to $A = 0.65$, $B = 0.76$ obtained from the LS coupling scheme for the pure $^2F_{5/2}$ term. The difference between these numbers indicates the SO coupling with the excited $^2F_{7/2}$ term.

From the model wavefunction, Equations 2a and 2b give analytic expressions for the orbital and spin magnetizations listed in Table 1. The spin magnetization $m_{\parallel}^S(\mathbf{r})$ represents an admixture of f_σ and f_π . As seen in Table S6 in the SI, the two contributions are of almost equal weights with opposite spin, leading to a very small expectation value $\langle S_{\parallel} \rangle = 0.04$. An isosurface plot of $m_{\parallel}^S(\mathbf{r})$ is shown in Figure 1. Due to f_σ and f_π contributions, the shape of $m_{\parallel}^S(\mathbf{r})$ is prolate but

reveals alternating blue and orange lobes. The blue lobes correspond to positive contributions related to f_σ (integrating to 0.27), whereas the orange lobes indicate negative contributions, here from f_π (-0.23). The fact that there are alternating signs in the plots means that the contributions cancel upon integration. The $4f$ electron density associated with the GS of $\text{Ce}(\text{COT})_2^-$ is shown in Figure 2 and is also found to be prolate in agreement with the function $R(\theta)$ of the $M_J = 1/2$ component of the Ce^{3+} free ion.¹⁴ Indeed, as shown in Figure S6 in the SI, only the natural orbitals $4f_\sigma$ and $4f_\pi$ are occupied and contribute to the density. Interestingly, the characterization of the $M_J = 1/2$ doublet as the GS of $\text{Ce}(\text{COT})_2^-$ is in contradiction with the qualitative model made by Rinehart and Long (R&L), where the association of a sandwich-type ligand geometry with the oblate shape of the Ce^{III} free-ion should maximize the anisotropy of the complex and should lead to a GS with a larger M_J value.¹⁴

For $m_{\parallel}^L(\mathbf{r})$ there are only contributions from the f_π orbitals, as expected, causing a positive $\langle L_{\parallel} \rangle = 0.46$. In total, the magnetic moment for a field in \parallel direction is mainly due to the orbital moment L_{\parallel} from the f_π orbitals. Due to the small orbital angular momentum projection m_ℓ , it causes a relatively small electronic g -factor of magnitude $g_{\parallel} = 1.07$, which compares well with the experimental value of $g_{\parallel} = 1.12$.²⁵ The magnetizations generated from the *ab-initio* wavefunction

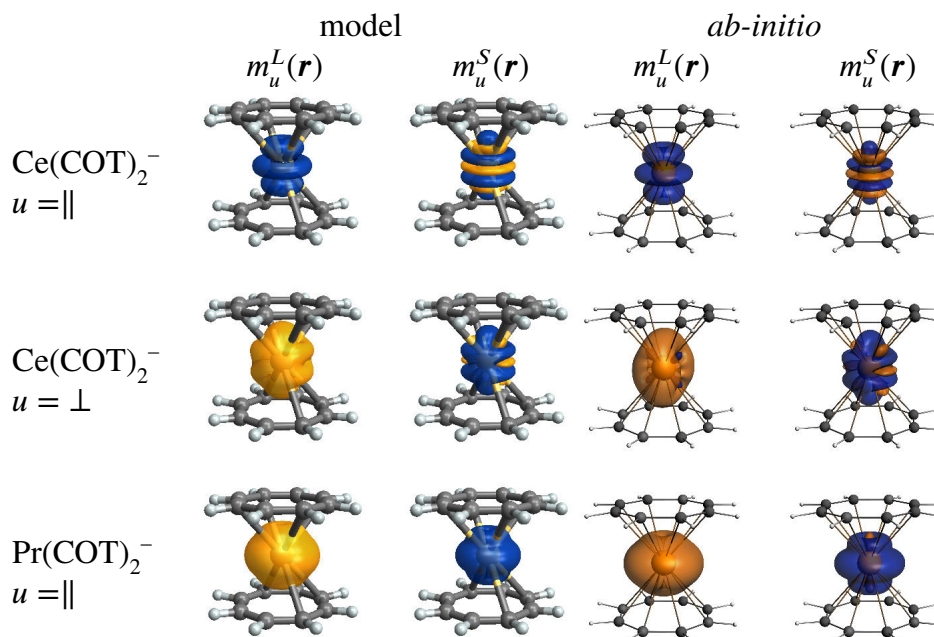


Figure 1: Isosurfaces (± 0.001 au.) of $m_u^L(\mathbf{r})$ and $m_u^S(\mathbf{r})$ for $\text{Ce}(\text{COT})_2^-$ and $\text{Pr}(\text{COT})_2^-$ obtained (a) with the model functions given in Table 1 and the parameters extracted from the *ab-initio* calculations, (b) and from the *ab-initio* calculations. In order to generate the visualizations, the spherical harmonics were multiplied with a normalized $4f$ Slater-type radial function using an exponent of 3.1 and 3.8 atomic units for Ce and Pr, respectively.

are also shown in Figure 1 and agree very well with the model.

This analysis clearly shows the utility of the *ab-initio* calculations (or magnetizations derived from CF wavefunctions, in situations where there is no metal-ligand covalency) for studying the magnetic properties of such complexes. The sole use of a CF-model derived angular dependence of the $4f$ charge density, or the use of non-multi-reference computations, for the rationalization of the magnetic behavior may lead to incorrect interpretations. For instance, an attempt was made recently to rationalize the GS of $\text{Ce}(\text{COT})_2^-$ by Kohn-Sham (KS) DFT calculations with a single occupation of the $4f_\delta$ orbital ($m_\ell = \pm 2$).⁵⁴ In the article, the authors postulate "... the Ce^{III} ion having an oblate electronic density ... the COT ligands provide strong equatorial interactions and this leads to stabilization of $m_J | \pm 1/2 \rangle$ as the ground state. DFT calculations also capture this point where the unpaired electron of Ce^{III} occupies the $4f_{xyz}$ orbital, leading to a cube-shape spin density". It is evident from Table 1 that the unpaired $4f$ orbital of the $M_J = 1/2$ GS cannot be the $4f_{xyz}$ orbital, which is a real linear combination of the $4f_\delta$ eigenfunctions of \hat{L}_z . First, the M_J quantum number is not compatible with unpaired $4f_\delta$ orbitals. Second, the linear symmetry demands that a state deriving from $4f_\delta$ is orbitally degenerate, meaning equal populations of the two $4f_\delta$ NOs generated from a multi-determinant wavefunction, or a KS reference with equal fractional occupations of the two $4f_\delta$, resulting in a cylindrically symmetric $4f$ charge density. Instead, in the GS the unpaired electron is shared among the $4f_\sigma$ and $4f_\pi$ orbitals due the SO coupling, with a $4f_\pi$ orbital degeneracy that also cannot be captured without a fractional-occupations KS reference. The resulting orbital and spin magnetizations of $M_J = 1/2$ shown in Figure 1 do not have a "cubic-shape" but are mainly prolate, and their integrations leads to g -factors that are in good agreement with those measured by Walter *et al.* in 2009.²⁵ We note in passing that previous DFT calculations performed by Ferraro *et al.* were able to converge to a solution where the unpaired orbital was the $4f_\sigma$.²⁶ From the *ab-initio* calculation, the $M_J = \pm 3/2$ doublet, 42% $^2\Delta$ in character, is found 1040 cm^{-1} above the GS, and the $M_J = \pm 5/2$ doublet at 561 cm^{-1} (see Table S7). This calculated energetic splitting of the $^2F_{5/2}$ multiplet is very reasonable, because the computed magnetic susceptibility χT is in very good agreement with experimental data (Figure 3). As suggested by experimental work,²⁵ the relative large energy gap between the GS and the first excited doublets leads to an essentially linear behavior of χT .

For the magnetic axis x (the \perp direction), the spin magnetization mainly arises from a spin-up contribution of the f_σ (integrating to +0.27) and one of the f_π (+0.11) orbital, giving the main blue lobe of the plot of $m_\perp^S(\mathbf{r})$. The orange lobes in $m_\perp^S(\mathbf{r})$ correspond to a negative contribution (-0.11) from the second f_π orbital. By integration, the two contributions from f_π cancel and the f_σ contribution gives $\langle S_\perp \rangle = 0.27$. A much larger orbital angular momentum expectation value is calculated for the \perp direction, with $\langle L_\perp \rangle = -1.72$. This large value arises from reinforcing negative contributions from the f_σ and f_π orbitals. It is interesting to underline that in $\text{Ce}(\text{COT})_2^-$,

Table 1: Model wave functionsⁱ $|\psi\rangle$ in the $|^{2S+1}L; M_J\rangle$ notation, orbital $m_u^L(\mathbf{r})$ and spin $m_u^S(\mathbf{r})$ magnetizations for $\text{Ce}(\text{COT})_2^-$ and $\text{Pr}(\text{COT})_2^-$.

$\text{Ce}(\text{COT})_2^-$			
ψ	$= A^2\Sigma_{1/2} - B^2\Pi_{1/2} \quad (u = \parallel)$	ψ	$= \frac{1}{\sqrt{2}}[A^2\Sigma_{1/2} - B^2\Pi_{1/2} + A^2\Sigma_{-1/2} - B^2\Pi_{-1/2}] \quad (u = \perp)$
$m_{\parallel}^S(\mathbf{r})$	$= \frac{A^2}{2}f_{\sigma}^2 - \frac{B^2}{4}[f_{\pi+}^2 + f_{\pi-}^2]$	$m_{\perp}^S(\mathbf{r})$	$= \frac{A^2}{2}f_{\sigma}^2 - \frac{B^2}{4}[f_{\pi-}^2 - f_{\pi+}^2]$
$m_{\parallel}^L(\mathbf{r})$	$= \frac{B^2}{2}[f_{\pi+}^2 + f_{\pi-}^2]$	$m_{\perp}^L(\mathbf{r})$	$= -\frac{AB\sqrt{12}}{2}f_{\sigma}^2 - AB\sqrt{3}f_{\pi+}^2$
$\text{Pr}(\text{COT})_2^-$			
ψ	$= A^3\Gamma_{-3} + B^3\Phi_{-3} + C^3\Delta_{-3} \quad (u = \parallel)$		
$m_{\parallel}^S(\mathbf{r})$	$= \frac{A^2}{4}[f_{\phi+}^2 + f_{\phi-}^2 + f_{\pi+}^2 + f_{\pi-}^2] - \frac{C^2}{6}[f_{\delta+}^2 + f_{\delta-}^2] - \frac{C^2}{3}f_{\sigma}^2 - \frac{C^2}{6}[f_{\phi+}^2 + f_{\phi-}^2 + f_{\pi+}^2 + f_{\pi-}^2]$		
$m_{\parallel}^L(\mathbf{r})$	$= -A^2[f_{\phi+}^2 + f_{\phi-}^2 + f_{\pi+}^2 + f_{\pi-}^2] - \frac{3B^2}{2}[\frac{2}{3}[f_{\sigma}^2 + \frac{1}{2}(f_{\phi+}^2 + f_{\phi-}^2)] + \frac{1}{6}[f_{\delta+}^2 + f_{\delta-}^2 + f_{\pi+}^2 + f_{\pi-}^2]]$ $-C^2[\frac{2}{3}[f_{\sigma}^2 + \frac{1}{2}(f_{\delta+}^2 + f_{\delta-}^2)] + \frac{1}{6}[f_{\phi+}^2 + f_{\phi-}^2 + f_{\pi+}^2 + f_{\pi-}^2]]$		

ⁱ Notation: Angular behavior only. The real tesseral harmonics $f_{\ell\pm}^{|m|}$ are the usual real linear combinations of the complex spherical harmonics $Y_{\ell}^{m\ell}$. For details see the Supplementary Information. Real coefficients A, B, C . Normalization implies $A^2 + B^2 = 1$ for $\text{Ce}(\text{COT})_2^-$ and $A^2 + B^2 + C^2 = 1$ for $\text{Pr}(\text{COT})_2^-$.

the magnetization is planar with $g_{\perp} > g_{\parallel}$.

The ground state of $\text{Pr}(\text{COT})_2^-$ is a non-Kramers doublet with $M_J = \pm 3$, deriving from the 3H_4 term of the Pr^{3+} free ion. As seen in Table 1, the wave function of the component with a magnetic moment along the \parallel direction corresponds to a mix of LS states $|^{2S+1}L; M_S\rangle : |^3\Gamma; 1\rangle$ ($A = 0.806$), $|^3\Phi; 0\rangle$ ($B = 0.529$) and $|^3\Delta; -1\rangle$ ($C = 0.200$). This composition is close to the pure $M_J = -3$ component of the 3H_4 multiplet, where $A = 0.809$, $B = -0.509$ and $C = 0.233$. The magnetic moment in \perp direction vanishes, as it does, or nearly does, for the remainder of the $\text{Ln}(\text{COT})_2^-$ series. Therefore, only the \parallel direction is discussed. As seen in Figure S6 in the SI, the two unpaired electrons in the GS of $\text{Pr}(\text{COT})_2^-$ occupy principally the $4f_{\phi}$ and $4f_{\delta}$ orbitals, and to a lesser extent the $4f_{\sigma}$ orbital. Consequently, the $4f$ electron density and $R(\theta)$ shown in Figure 2 are mainly oblate. Interestingly, the shape of the orbital and spin magnetizations differ from the electronic density with a more oblate orbital magnetization and a more prolate spin magnetization.

The spin expectation value $\langle S_{\parallel} \rangle = 0.61$ is mainly due to the contribution from $|^3\Gamma; 1\rangle$. Indeed, f_{ϕ} and f_{π} orbitals of the $|^3\Gamma; 1\rangle$ term contribute equally and with positive spin to m_{\parallel}^S . This gives the blue lobe in Figure 1. $m_{\parallel}^S(\mathbf{r})$ also gives a small axial orange lobe due to the negative contribution from the f_{σ} and f_{δ} orbitals of the $|^3\Delta; -1\rangle$ term. The angular expectation value $\langle L_{\parallel} \rangle = -3.61$ arises mainly from f_{ϕ} contributions to m_{\parallel}^L from the $|^3\Gamma; 1\rangle$ and $|^3\Phi; 0\rangle$ components in the wavefunction. The total magnetic moment in \parallel direction is large because m_{\parallel}^L is only partially canceled by m_{\parallel}^S . The result is a pronounced magnetic anisotropy, as evident from the g -factors (Table 2).

4 Magnetic moments of $\text{Ln}(\text{COT})_2^-$

The $4f$ electron densities and the magnetizations for the \parallel magnetic axis are shown in Figures 2 and 4 for the ground states of the $\text{Ln}(\text{COT})_2^-$ complexes. These densities are compared to the angular dependence $R(\theta)$ of the $4f$ density of the $|J, M_J\rangle$ states of the $\text{Ln}(\text{III})$ ions previously described by Sievers.¹⁵ Expectation values $\langle L_u \rangle$ and spin $\langle S_u \rangle$ and the associated electronic g -factors, are collected in Tables 2 and 3 for $u = \parallel, \perp$. Detailed assignments of low-energy parts of the electronic spectra, and CF parameters derived from the calculations, can be found in the SI.

4.1 L and S antiparallel

The Ce and Pr systems were already discussed. Compared to $\text{Pr}(\text{COT})_2^-$, the addition of one more electron in the $4f$ shell, as in $\text{Nd}(\text{COT})_2^-$, does not lead to an increase of the magnetic anisotropy of the GS. Indeed, the calculation gives a smaller $g_{\parallel} = 3.48$. In $\text{Nd}(\text{COT})_2^-$, the GS derives from the $M_J = \pm 5/2$ components of the Nd^{3+} multiplet $^4I_{9/2}$. According to Table S7, these components correspond to an admixture of SF wavefunctions deriving from $|^4\Gamma; -3/2\rangle$ (44 %) and $|^4\Phi; -1/2\rangle$ (37 %), due to SO coupling, characterized by $M_L = \pm 4$ and $M_L = \pm 3$, respectively. The expectation values $\langle L_{\parallel} \rangle = -3.25$ and $\langle S_{\parallel} \rangle = 0.75$ reflect this admixture of SF states and indicates the impact of the SO coupling. The GS of $\text{Pm}(\text{COT})_2^-$ derives from the $M_J = \pm 4$ components of the 5I_4 multiplet of Pm^{3+} . The dominant character (78%) of this doublet originates from the SF $|^5I; \pm 2\rangle$ state, which corresponds to single occupations of f_{σ} , f_{π} , f_{δ} and f_{ϕ} , giving a slightly prolate shape of the $4f$ -electron density. $\langle L_{\parallel} \rangle = -5.73$ is not far from $L = \pm 6$ expected for a SF 5I state, and $\langle S_{\parallel} \rangle = 1.73$ is not far from $S = 2$ of a pure quintuplet. Due to SO coupling, the GS also contains a sizable admixture of SF $|^5H; \pm 1\rangle$ functions which reduces the magnitude of both expectation values relative to the SF limit. The shape of the magnetizations should not be taken as an indication for presence or lack of magnetic anisotropy since integration of these functions ultimately determines μ_{\parallel} . As already pointed out, in \perp direction, there is no magnetic moment

Table 2: Calculated $\text{Ln}(\text{COT})_2^-$ spin and orbital angular momentum expectation values and g -factors: Ce – Gd ^a

Ln =	Ce	Pr	Nd	Pm	Sm	Gd
$\langle L_{\parallel} \rangle$	0.461	-3.609	-3.250	-5.732	-4.735	0.002
$\langle L_{\perp} \rangle$	-1.716	0.000	-0.003	0.000	0.000	0.000
$\langle S_{\parallel} \rangle$	0.038	0.613	0.753	1.737	2.239	3.492
$\langle S_{\perp} \rangle$	0.269	0.000	0.001	0.000	0.000	0.000
$\pm g_{\parallel}$	1.074	4.765	3.485	4.505	0.505	13.989
$\pm g_{\perp}$	2.354	0.000	0.003	0.000	0.000	0.000

^a Eu data not listed because of calculated non-magnetic ground state

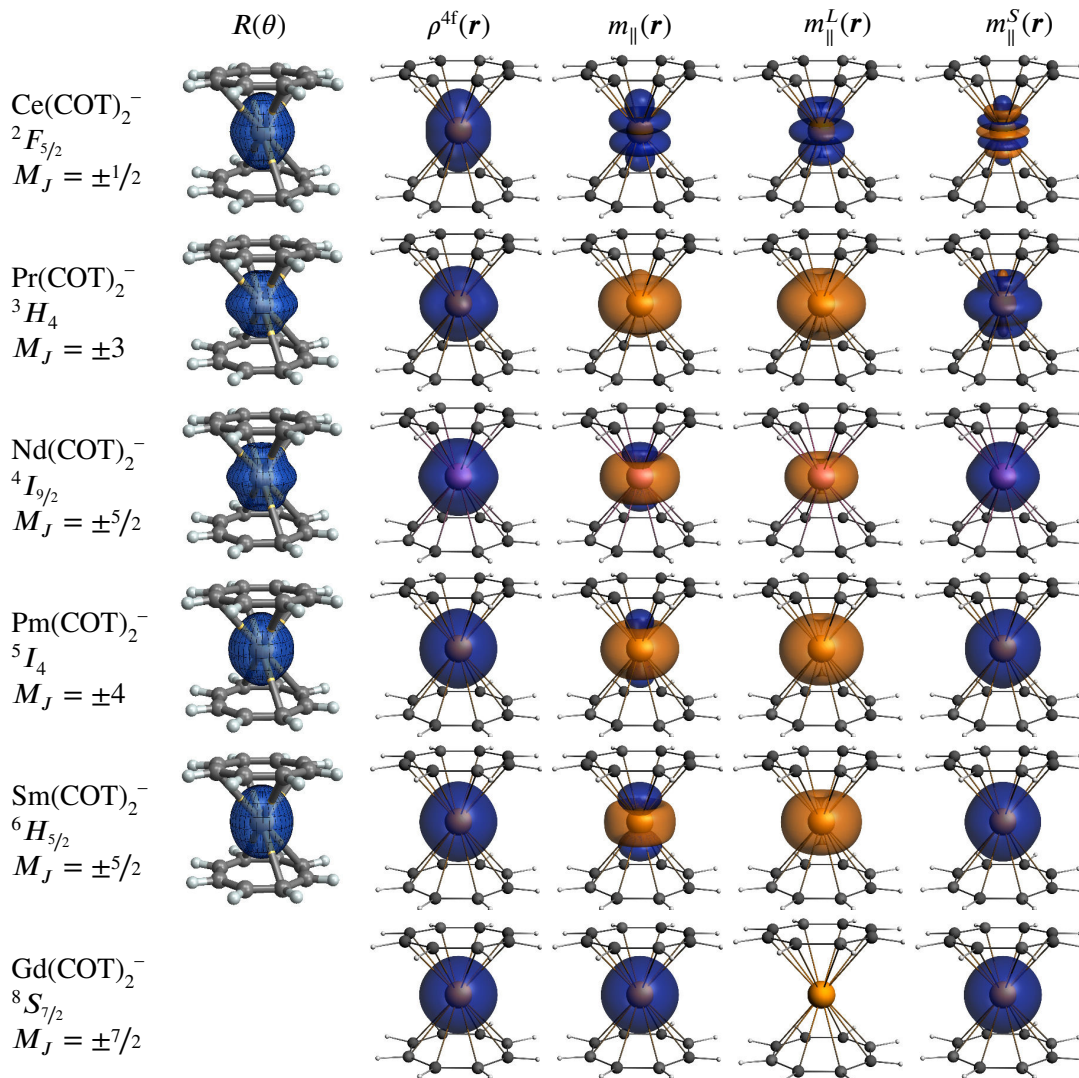


Figure 2: Angular dependence $R(\theta)$ of the $4f$ density according to Eq. 7,¹⁵ $4f$ electron density, and magnetizations for the magnetic axis \parallel , for $\text{Ln}(\text{COT})_2^-$ with $\text{Ln} = \text{Ce} - \text{Gd}$. Eu data are not shown because of calculated non-magnetic ground state. Isosurfaces at ± 0.001 au.

and therefore there is considerable axial anisotropy. Rather, the shapes of $m_{\parallel}^S(\mathbf{r})$ and $m_{\parallel}^L(\mathbf{r})$ reflect the contributions of π , δ and ϕ (and σ , in the case of $m_{\parallel}^S(\mathbf{r})$). Interestingly, the sandwich-type ligand geometry in $\text{Pr}(\text{COT})_2^-$ leads to a GS with the largest M_J value and a pronounced prolate $4f$ -electron density.

The GSs of $\text{Sm}(\text{COT})_2^-$ and $\text{Eu}(\text{COT})_2^-$ afford among the smallest magnetic anisotropies in the $\text{Ln}(\text{COT})_2^-$ series. Interestingly, these small magnetic moments have different origins. In $\text{Sm}(\text{COT})_2^-$, the GS derives from the $M_J = \pm 5/2$ components of the ${}^6H_{5/2}$ multiplet of Sm^{3+} . The main character of these M_J components arise from the SF 6H state (81 %), which corresponds to an orbital occupation $f_{\sigma}f_{\pi}^2f_{\delta}f_{\phi}$ with $M_L = 5$. The *ab-initio* angular momentum expectation

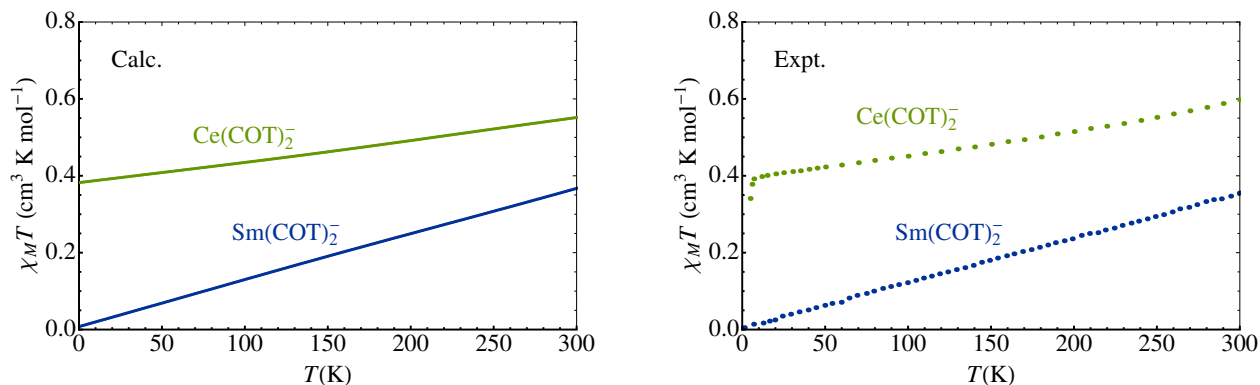


Figure 3: Calculated (left) and experimental (right) molar magnetic susceptibility $\chi_M T$ ($\text{cm}^3 \text{K mol}^{-1}$) of selected $\text{Ln}(\text{COT})_2^-$ complexes ($\text{Ln} = \text{Ce}$ and Sm). The experimental data were extracted from graphical material in Reference 25 for $\text{Ce}(\text{COT})_2^-$ and Reference 36 for $\text{Sm}(\text{COT})_2^-$.

values are not far from what is expected for an idealized $\text{SF } ^6H$ micro-state: $\langle L_{\parallel} \rangle = -4.73$ vs. $M_L = \pm 5$ for 6H ; $\langle S_{\parallel} \rangle = -2.24$ vs. $M_S = \pm 5/2$ for a spin sextuplet. Due to their opposite signs, the magnetic moment along the \parallel axis of $\text{Sm}(\text{COT})_2^-$ is very small, resulting in an overall small magnetic anisotropy. The $M_J = -5/2$ component of a pure $^6H_{5/2}$ term has a composition of 54 % $|^6H; -5/2\rangle$, and 27 % $|^6\Gamma; -3/2\rangle$ which strongly differs from the ab initio numbers (see Table S7). As seen in Figure 3, the small magnitude of the magnetic moment leads to a relatively small isotropic magnetic susceptibility χT which is nearly linear in T , meaning that χ is dominated by a temperature-independent contribution. This linear behavior of χT is caused by a large second-order Zeeman coupling between the GS and the $^6H_{7/2}$ state at 985 cm^{-1} above the GS.

For $\text{Eu}(\text{COT})_2^-$, the situation differs. Here, the GS is a non-degenerate state deriving from the 7F_0 term of Eu^{3+} . Accordingly, there is neither spin nor angular momentum due to the lack of orbital and spin degeneracy. In $\text{Gd}(\text{COT})_2^-$ all of the $4f$ orbitals are singly occupied, giving rise to a GS deriving from the $^8S_{7/2}$ multiplet of Gd^{3+} in which the orbital angular momentum is completely quenched. The electronic density of the $4f$ shell as well as m_{\parallel}^S and the total magnetization are the same for this electronic state and essentially spherical. As seen in Table 2, $\text{Gd}(\text{COT})_2^-$ affords a large $g_{\parallel} = 14.98$. It arises purely from the spin expectation value $\langle S_{\parallel} \rangle = 3.49$. The calculated value is basically identical to $S = 7/2$ of an idealized spin octuplet.

4.2 L and S parallel

In the second half of the $\text{Ln}(\text{COT})_2^-$ series, L and S are parallel which is reflected by the plots of the orbital and spin magnetization in Figure 4 having the same color. The reinforcing magnetic moments lead to large magnetic moments in \parallel direction and therefore large magnetic anisotropy. The exception is $\text{Tb}(\text{COT})_2^-$. Here, CF splitting of the Tb^{3+} GS multiplet 7F_6 favors a singlet

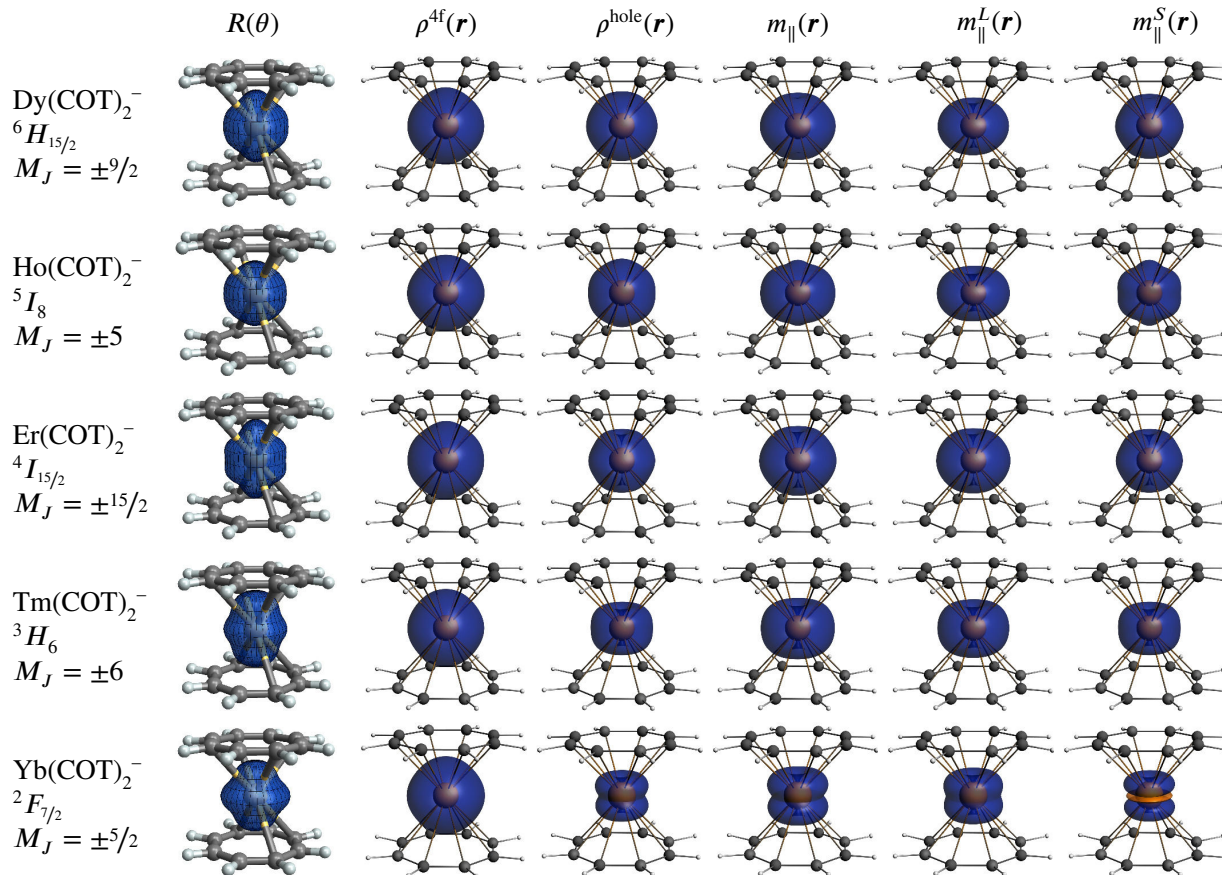


Figure 4: Angular dependence $R(\theta)$ of the $4f$ density according to Eq. 7,¹⁵ $4f$ electron density, and magnetizations for the magnetic axis \parallel , for $\text{Ln}(\text{COT})_2^-$ with $\text{Ln} = \text{Tb} - \text{Yb}$. Tb data are not shown because of calculated non-magnetic ground state. Isosurfaces at ± 0.001 au.

ground state characterized by $M_J = 0$. The lack of orbital and spin degeneracy therefore leads to vanishing magnetic moments in the GS. Despite a non magnetic GS, $\text{Tb}(\text{COT})_2^-$ exhibits relatively large magnetic susceptibility due to the presence of low-lying excited doublets (Figure 5).

Table 3: Calculated $\text{Ln}(\text{COT})_2^-$ spin and orbital angular momentum expectation values and g -factors: Dy – Yb ^a

Ln =	Dy	Ho	Er	Tm	Yb
$\langle L_{\parallel} \rangle$	3.021	3.762	6.020	5.003	2.136
$\langle L_{\perp} \rangle$	0.013	0.000	0.000	0.000	0.006
$\langle S_{\parallel} \rangle$	1.475	1.237	1.476	0.993	0.316
$\langle S_{\perp} \rangle$	0.007	0.000	0.000	0.000	0.001
$\pm g_{\parallel}$	11.949	12.479	17.953	13.986	5.719
$\pm g_{\perp}$	0.055	0.000	0.000	0.000	0.016

^a Tb data not listed because of calculated non-magnetic ground state

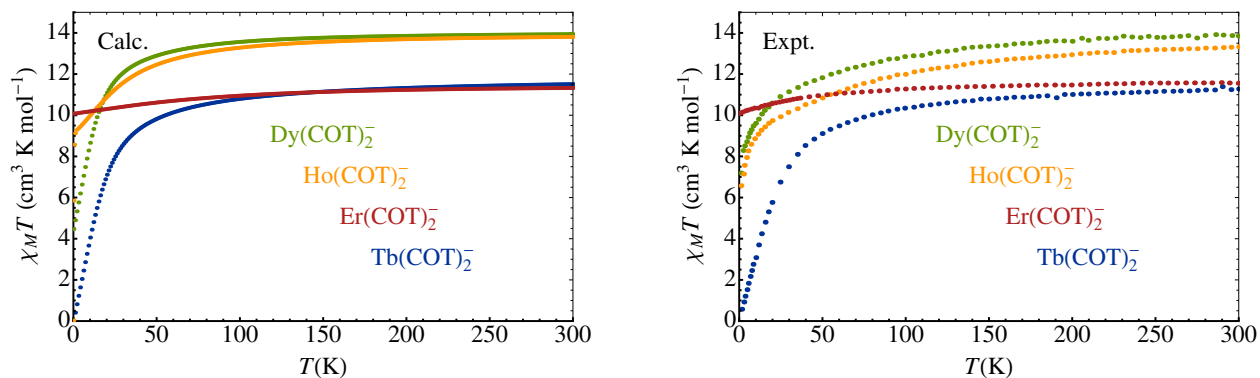


Figure 5: Calculated (left) and experimental (right) molar magnetic susceptibility $\chi_M T$ ($\text{cm}^3 \text{K mol}^{-1}$) of selected $\text{Ln}(\text{COT})_2^-$ complexes ($\text{Ln} = \text{Tb, Dy, Ho}$ and Er). The experimental data were extracted from graphical material in Reference 37 for $\text{Er}(\text{COT})_2^-$, and Reference 36 for $\text{Dy}(\text{COT})_2^-$, $\text{Ho}(\text{COT})_2^-$ and $\text{Tb}(\text{COT})_2^-$.

The singlet GS leads to a linear behavior of χT at low temperature, characteristic of temperature independent paramagnetism (TIP) behavior. The thermal population of the magnetic doublets $M_J = \pm 1$ and ± 2 , found at 40 and 161 cm^{-1} above the GS, respectively, leads to a $1/T$ dependence of χ at higher temperature and a plateau for χT .

A large magnetic moment μ_{\parallel} is calculated for the GS of $\text{Dy}(\text{COT})_2^-$ with $\langle L_{\parallel} \rangle = 3.021$ and $\langle S_{\parallel} \rangle = 1.475$. In $\text{Dy}(\text{COT})_2^-$, the GS corresponds to the $M_J = \pm 9/2$ components of the ${}^6H_{15/2}$ of Dy^{3+} . Due to the SO coupling, the GS has a strong admixture of the SF ${}^6\Phi$, ${}^6\Delta$ and ${}^6\Gamma$ states. All the seven $4f$ orbitals contribute to some extent to the magnetic moment μ_{\parallel} . A non-zero but small magnetic moment is also calculated along the \perp axis, characterized by the shape of $m_{\perp}^L(\mathbf{r})$ and $m_{\perp}^S(\mathbf{r})$ shown in the SI. These densities have magnitudes smaller by a factor of 1/10 compared to the \parallel direction, and their integration leads to angular momentum expectation values very close to zero because of cancellation of positive and negative contributions. It is possible that a slight symmetry breaking of the wavefunction leads to the non-vanishing $m_{\perp}^{L/S}(\mathbf{r})$. The $\text{Dy}(\text{COT})_2^-$ GS affords a large magnetic anisotropy characterized by $g_{\parallel} = 11.94$ and $g_{\perp} = 0.05$.

Due to SO coupling, the GS of $\text{Ho}(\text{COT})_2^-$, characterized by the $M_J = \pm 5$ components of the 5I_8 multiplet, exhibits also a strong admixture of SF states. This admixture is reflected in the magnitude of the expectation values $\langle L_{\parallel} \rangle = 3.76$ and $\langle S_{\parallel} \rangle = 1.24$ close to the values for the pure $M_J = \pm 5$ of the 5I_8 multiplet: 3.75 and 1.25, respectively. The orbital and spin angular expectation values are exactly equal to zero along the \perp axis, leading to a GS with a relatively large magnetic anisotropy. Compared to $\text{Dy}(\text{COT})_2^-$, which is a Kramers doublet, the GS of $\text{Ho}(\text{COT})_2^-$ correspond to a non-Kramers doublet.

The GS of $\text{Er}(\text{COT})_2^-$ exhibits the largest magnetic anisotropy in the $\text{Ln}(\text{COT})_2^-$ series with $g_{\parallel} = 17.95$ and $g_{\perp} = 0.00$. Here the GS derives from the $M_J = \pm 15/2$ components of the ${}^4I_{15/2}$

multiplet of Er^{3+} . Due to the change of sign in the Stevens parameters $\beta_J(n)$, it is interesting to notice that the energetic ordering of the M_J components in $\text{Er}(\text{COT})_2^-$ is reversed compared to the ones in $\text{Dy}(\text{COT})_2^-$; both derive from the $J = 15/2$ manifold. This reordering has a strong impact on the GS magnetic moments. The GS $M_J = \pm 15/2$ components for $\text{Er}(\text{COT})_2^-$ are essentially of a pure SF $|^4I; \pm 5/2\rangle$ (98%) character. The three unpaired electrons are described by f_π , f_δ and f_ϕ orbitals (see Figure S5 of SI), leading to relatively spherical $4f$ -electron density. The $\langle L_\parallel \rangle = 6.02$ and $\langle S_\parallel \rangle = 1.47$ values are very close to the pure LS term. The shape of $m_\parallel^L(\mathbf{r})$ and $m_\parallel^S(\mathbf{r})$ reflect this addition of the f_π , f_δ and f_ϕ contributions as well as the lack of a contribution from f_σ to the spin magnetization (Figure S7). Figure 6 shows the difference between the electron densities of the $M_J = 15/2$ and $M_J = 1/2$ doublets. The density of the $M_J = 15/2$ state is slightly prolate while the one of the $M_J = 1/2$ is slightly oblate, as already pointed out by R&L.¹⁴ This difference in the electron distribution, which is amplified in $R(\theta)$, goes along with a re-orientation of the magnetic anisotropy between the Kramers doublets. For the GS $M_J = \pm 15/2$, the prolate density goes along with an anisotropy axis oriented along the COT centroid, whereas the oblate density of the $M_J = 1/2$ doublet goes along with a planar anisotropy. Along the \perp axis, the magnetic moment of the GS vanishes, giving rise a large axial anisotropy. On the contrary, for $M_J = 1/2$ a large magnetic moment is calculated along the \perp axis with $g_\perp = 9.65$.

The calculated magnetic susceptibilities χT of the Dy, Ho, and Er complex are shown in Figure 5, together with χT of $\text{Tb}(\text{COT})_2^-$, and compared to experimental data. The calculations reproduce properly the experimental curves, both in term of the overall shapes and the magnitudes at room temperature. The presence of a magnetic GS for Dy, HO and Er renders the analysis somewhat more complex compared to the case of Tb. For instance, for $\text{Er}(\text{COT})_2^-$ the presence of a first excited state with a small magnetic moment, i.e. $M_J = 1/2$, should lead to a decrease of the susceptibility with increasing T via the Boltzmann average of the first-order Zeeman interactions. However, this decrease is counterbalanced by the second-order Zeeman interaction within the other M_J levels, leading to a small increase of χT with temperature. On the contrary, for $\text{Dy}(\text{COT})_2^-$ and $\text{Ho}(\text{COT})_2^-$ there are excited states with larger magnetic moments accessible at low energies (see Table S8). The population of these excited states leads to a rapid increase of χT with temperature. The *ab-initio* calculations very likely underestimate the energy gap between the GS and the first excited doublet for $\text{Ho}(\text{COT})_2^-$ (the states are practically degenerate in the calculation), causing an overestimation of the susceptibility at very low temperatures.

The non-Kramers doublet GS of $\text{Tm}(\text{COT})_2^-$ is also characterized by a large axial magnetic anisotropy with $g_\parallel = 13.98$ and $g_\perp = 0.00$. The GS here derives from the $M_J = \pm 6$ components of the 3H_6 multiplet of Tm^{3+} , meaning that M_J is as large as possible for this multiplet. As for the Er complex, the GS is almost a pure SF term $|^3H, 1\rangle$ with M_L and M_S maximal and of the same sign. The *ab-initio* expectation values are again very close to those of the idealized SF term with

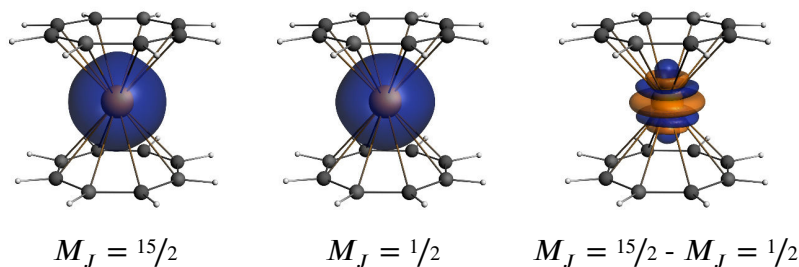


Figure 6: $\text{Er}(\text{COT})_2^-$: $4f$ electron density for $M_J = \pm 15/2$, $M_J = \pm 1/2$. Isosurfaces at ± 0.001 au.

$\langle L_{\parallel} \rangle = 5.00$ and $\langle S_{\parallel} \rangle = 0.99$. The two unpaired electrons are described by f_{δ} and f_{ϕ} orbitals, and thus the shapes of the orbital and spin magnetizations reflect the addition of the f_{δ} and f_{ϕ} contributions whereas the $4f$ density and $R(\theta)$ reflect the double occupations of f_{σ} and the f_{π} set.

Finally, a much smaller magnetic anisotropy is calculated for the GS of $\text{Yb}(\text{COT})_2^-$ where $g_{\parallel} = 5.72$ and $g_{\perp} = 0.02$. The GS is a Kramers doublet deriving from the $M_J = \pm 5/2$ components of the ${}^2F_{7/2}$ multiplet of Yb^{3+} . It corresponds to an admixture of the SF states $|{}^2\Delta; \pm 1/2\rangle$ (86 %) and $|{}^2\Phi; \mp 1/2\rangle$ close to the composition of the pure $M_J = 5/2$ of ${}^2F_{7/2}$ (86 % and 14 %). The unpaired electron is mainly described by the f_{δ} orbitals (Figure S7), which is clearly reflected in the shapes of the orbital and spin magnetizations. Due to the SO coupling, the f_{ϕ} orbitals influence the magnetic moment. In terms of Yb^{3+} , this is a contribution from SF $|{}^2\Phi; \pm 1/2\rangle$, which shows up, for example, as the orange equatorial lobe in $m_{\parallel}^S(\mathbf{r})$. $\langle L_{\parallel} \rangle = 2.14$ and $\langle S_{\parallel} \rangle = 0.32$ are very close to the idealized values expected for the $M_J = 5/2$ component of the ${}^2F_{7/2}$ term (2.14 and 0.36). As for the other complexes in the second half of the Ln series, μ_{\parallel} and g_{\parallel} are dominated by the orbital angular momentum but re-enforced by the spin.

4.3 $4f$ electron density versus magnetization

For further analysis we select two of the complexes, namely $\text{Nd}(\text{COT})_2^-$ and $\text{Er}(\text{COT})_2^-$, and investigate the states with different M_J deriving from the Ln^{3+} ground state terms. The $4f$ electron density, the total magnetization and its orbital and spin contributions for the different M_J components of the ground multiplets of $\text{Nd}(\text{COT})_2^-$ and $\text{Er}(\text{COT})_2^-$ are shown in Figures 7 and 8, respectively. These densities are compared to the angular dependence function $R(\theta)$ of the corresponding $4f$ densities determined by Sievers for the Ln(III) free ions and recently utilized by R&L in the context of SMM design.^{14,15}

In $\text{Nd}(\text{COT})_2^-$, the shape of the $R(\theta)$ functions accentuates the more subtle changes in the $4f$ electron densities of the different $|J, M_J\rangle$ states calculated from *ab-initio* wave functions. The reader is reminded that the $R(\theta)$ functions contain a monopole moment of $3/4\pi$ which intention-

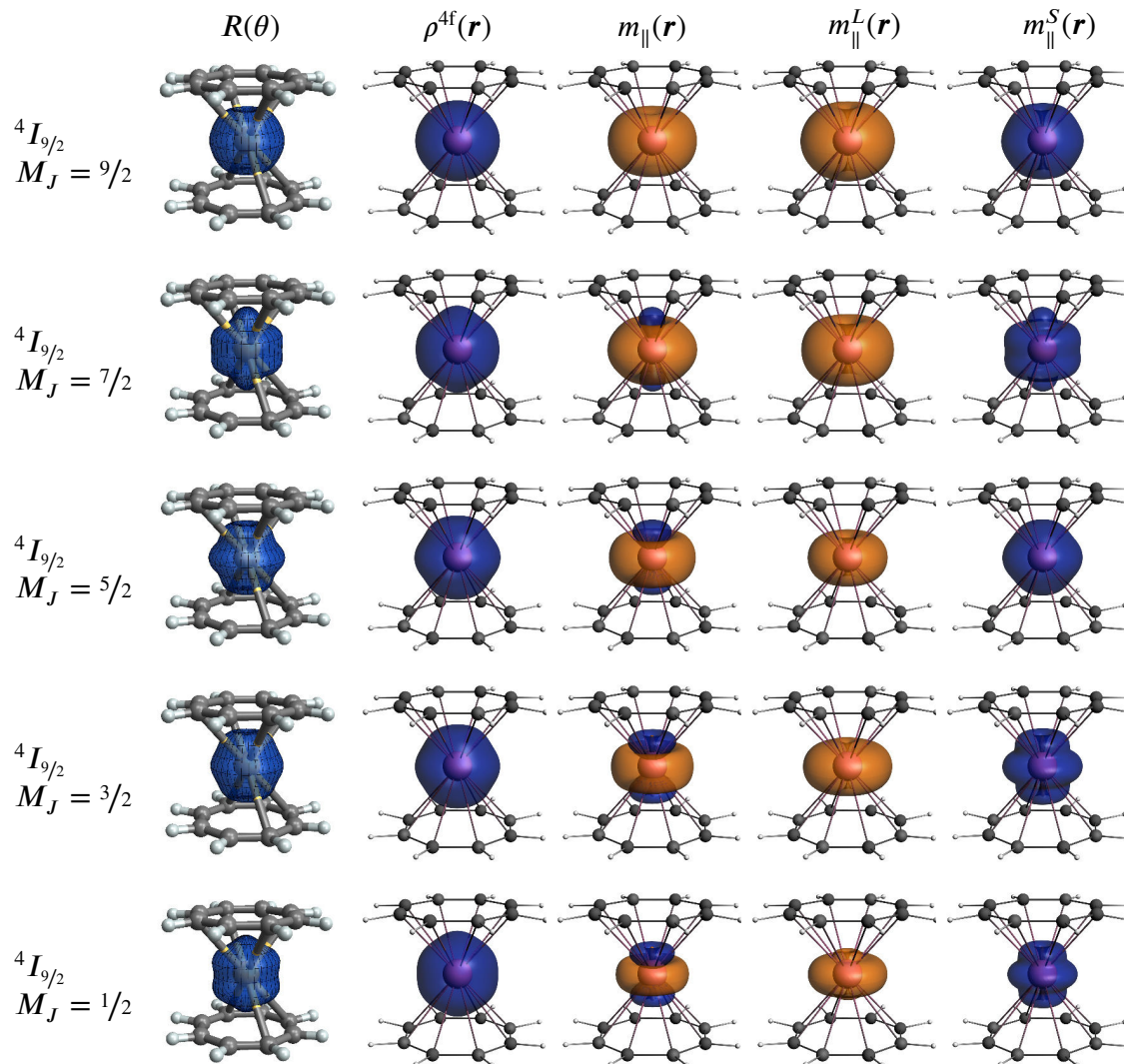


Figure 7: $\text{Nd}(\text{COT})_2^-$: Angular dependence $R(\theta)$ of the 4f density according to Eq. 7,¹⁵ 4f electron density, and magnetizations for the magnetic axis \parallel . Isosurfaces at ± 0.001 au.

ally leads to a more drastic representation of the asphericities of the densities.¹⁵ The appearance of $\rho^{4f}(\mathbf{r})$ is directly related to the occupation of the 4f NOs which are given in Table 4 for $\text{Nd}(\text{COT})_2^-$. A prolate shape of the electron density is associated with larger occupations of the orbitals with small $|m_\ell|$ versus large $|m_\ell|$, while for an oblate density the opposite is the case, irrespective of the contributions of small $|m_\ell|$ versus large $|m_\ell|$ to the spin magnetization. For instance, the pronounced axial shape of $\rho^{4f}(\mathbf{r})$ for the $M_J = 1/2$ and $7/2$ components is due to the largest occupation number of the $4f_\sigma$ orbital in the $^4I_{9/2}$ term, with 0.57 and 0.67 electrons, respectively. For the $M_J = 9/2$ component, the oblate shape of the electron density is associated with larger occupation of the $4f_\delta$ and $4f_\phi$ orbitals. The other M_J components are not straightforwardly described as prolate or oblate because of the small $4f_\sigma$ but large $4f_\pi$ occupations. Even for the $M_J = 1/2$

component, the large f_δ occupation somewhat obscures the classification.

As seen in Figure 2, the total magnetization somewhat follows the shape of the electron density in the first half of the series. However, the distributions of the orbital and spin magnetizations cannot be deduced from the electron density alone. The fact that $m_{\parallel}^L(\mathbf{r})$ is typically oblate rather than not is easily understood because the $4f_\sigma$ orbital does not contribute to the \parallel orbital moment and consequently $m_{\parallel}^L(\mathbf{r})$ tends to be small in \parallel direction. For the smallest M_J values the orbital moment is small overall, and $m_{\parallel}^L(\mathbf{r})$ is mainly equatorially distributed, indicating a dominance of $4f_\phi$. When going to the largest M_J values, the orbital moment increases linearly. The oblate character of $m_{\parallel}^L(\mathbf{r})$ decreases somewhat with increasing M_J , indicating that orbital angular momenta from $4f_\delta$ and $4f_\pi$ are also contributing. There are competing trends, however, since with the increase of M_J the occupation of the $4f_\phi$ orbitals increases (Table 4), which in the plots of $m_{\parallel}^L(\mathbf{r})$ manifests as an overall increase in the equatorial (oblate) contribution. The large $|m_\ell|$ of the $4f_\phi$ orbitals thereby amplifies their contributions to $m_{\parallel}^L(\mathbf{r})$.

In this context it is worth mentioning that equal occupations of $1/2$ or $3/2$ of pairs of $4f$ orbitals with the same $|m_\ell|$ are able to maximize their contribution to $m_{\parallel}^L(\mathbf{r})$. For instance, the increase of the angular momentum expectation value in $\text{Er}(\text{COT})_2^-$, when going from the $M_J = 13/2$ component to $M_J = 15/2$, is associated with a decrease of the NO occupation of the $4f_\pi$ pair in favor of $4f_\sigma$. In $M_J = 15/2$, the NO occupation of the $4f_\pi$ pair is almost equal to $3/2$, and a linear combination of the two orbitals can be made which leads to a single occupation of an \hat{L}_z eigenfunction with maximum $\pm m_\ell$ value. In the case where the paired orbitals are singly or doubly occupied, the result can be written in terms of a sum of equally populated $+m_\ell$ and $-m_\ell$ eigenfunctions, and therefore, the orbital angular momentum contribution is quenched. This quenching of the orbital momentum occurs, for instance, for the ground state of $\text{Gd}(\text{COT})_2^-$ in which all the $4f$ NOs are singly occupied (see Table S4).

Table 4: $\text{Nd}(\text{COT})_2^-$: Occupation of the $4f$ NOs and spin populations of the $4f$ NSOs contributing to $2\langle S_{\parallel} \rangle$ for the M_J components of the ground multiplet.^a The angular and spin expectation values for the M_J components with $\langle S_{\parallel} \rangle > 0$ are also given.

M_J	NO Occupations				NSO Spin Populations				$\langle L_{\parallel} \rangle$	$\langle S_{\parallel} \rangle$
	$4f_\sigma$	$4f_\pi$	$4f_\delta$	$4f_\phi$	$4f_\sigma$	$4f_\pi$	$4f_\delta$	$4f_\phi$		
$1/2$	0.574	0.348	0.532	0.348	-0.030	0.163	0.015	0.092	-0.757	0.255
$3/2$	0.287	0.611	0.347	0.398	-0.064	0.388	0.142	0.243	-2.114	0.614
$5/2$	0.310	0.625	0.258	0.462	0.190	0.254	0.082	0.317	-3.250	0.753
$7/2$	0.677	0.298	0.372	0.490	0.554	-0.070	0.277	0.334	-4.312	0.818
$9/2$	0.298	0.379	0.488	0.497	-0.022	0.302	0.385	0.395	-5.562	1.072

^a For π , δ and ϕ , the NO populations and NSO spin populations are listed per orbital type, not per pair.

Similarly to the orbital magnetization, the spin magnetization is only indirectly related to $\rho^{4f}(\mathbf{r})$. An interesting example is the comparison of the $M_J = 1/2$ and $7/2$ components in $\text{Nd}(\text{COT})_2^-$. As already mentioned, the shape of the $4f$ electronic density is prolate in either case due to a large occupation of $4f_\sigma$. However, the contribution of $4f_\sigma$ to the spin angular momentum strongly differs between the two components, with contributions integrating to -0.03 and $+0.55$ for $M_J = 1/2$ and $7/2$, respectively. This means that in the former case the NO occupation is of the spin-compensated type whereas in the latter the occupation is mainly in the α -spin component. The differences in the f_σ spin populations lead to a more prolate shape of $m_{\parallel}^S(\mathbf{r})$ for the $M_J = 7/2$ component. In the first half of the $\text{Ln}(\text{COT})_2^-$ series, due to L and S being antiparallel, the total magnetization may contain positive and negative lobes as seen for the GS of $\text{Nd}(\text{COT})_2^-$, $\text{Pm}(\text{COT})_2^-$ and $\text{Sm}(\text{COT})_2^-$.

In $\text{Er}(\text{COT})_2^-$, the $4f$ electron densities also follow the shape of the $R(\theta)$ functions, but with much more subtle changes. The occupation numbers of the $4f$ shell for the different M_J components of the $^4I_{15/2}$ term are given in Table 5, and allow to rationalize the shape of $\rho^{4f}(\mathbf{r})$ for the different components. Due to a nearly doubly occupied $4f_\sigma$ orbital, the largest M_J component has a strong prolate density, whereas the oblate density of the smallest M_J state is associated with a large occupation of the $4f_\phi$ orbitals and a smaller occupation of the $4f_\sigma$ orbital. Contrary to $\text{Nd}(\text{COT})_2^-$, the shape of the magnetization in $\text{Er}(\text{COT})_2^-$, and likewise for the $\text{Ln}(\text{III})$ ions of the second half of the series, is not similar to the electronic density but resembles more closely the holes in the $4f$ the density. The maxima of density are found to the equatorial plane for large M_J , giving an oblate magnetization for $M_J = 15/2$, whereas the maxima of density are found in the poles for the small values of M_J , giving a prolate magnetization for $M_J = 1/2$. For the same

Table 5: $\text{Er}(\text{COT})_2^-$: Occupation of the $4f$ NOs and spin populations of the $4f$ NSOs contributing to $2\langle S_{\parallel} \rangle$ for the M_J components of the ground multiplet.^a The angular and spin expectation values for the M_J components with $\langle S_{\parallel} \rangle > 0$ are also given.

M_J	NO Occupations				NSO Spin Populations				$\langle L_{\parallel} \rangle$	$\langle S_{\parallel} \rangle$
	$4f_\sigma$	$4f_\pi$	$4f_\delta$	$4f_\phi$	$4f_\sigma$	$4f_\pi$	$4f_\delta$	$4f_\phi$		
$1/2$	1.352	1.725	1.399	1.700	0.117	-0.047	0.071	0.024	0.393	0.106
$3/2$	1.493	1.607	1.475	1.672	0.259	-0.070	0.176	0.079	1.186	0.315
$5/2$	1.688	1.439	1.593	1.623	0.200	0.063	0.194	0.154	1.988	0.511
$7/2$	1.790	1.341	1.696	1.567	0.024	0.292	0.147	0.245	2.802	0.696
$9/2$	1.675	1.421	1.719	1.521	-0.020	0.426	0.122	0.338	3.621	0.877
$11/2$	1.377	1.675	1.637	1.498	0.290	0.289	0.220	0.411	4.431	1.065
$13/2$	1.221	1.889	1.498	1.496	0.778	-0.020	0.448	0.453	5.225	1.270
$15/2$	1.999	1.507	1.497	1.495	0.000	0.492	0.488	0.496	6.020	1.476

^a For π , δ and ϕ , the NO populations and NSO spin populations are listed per orbital type, not per pair.

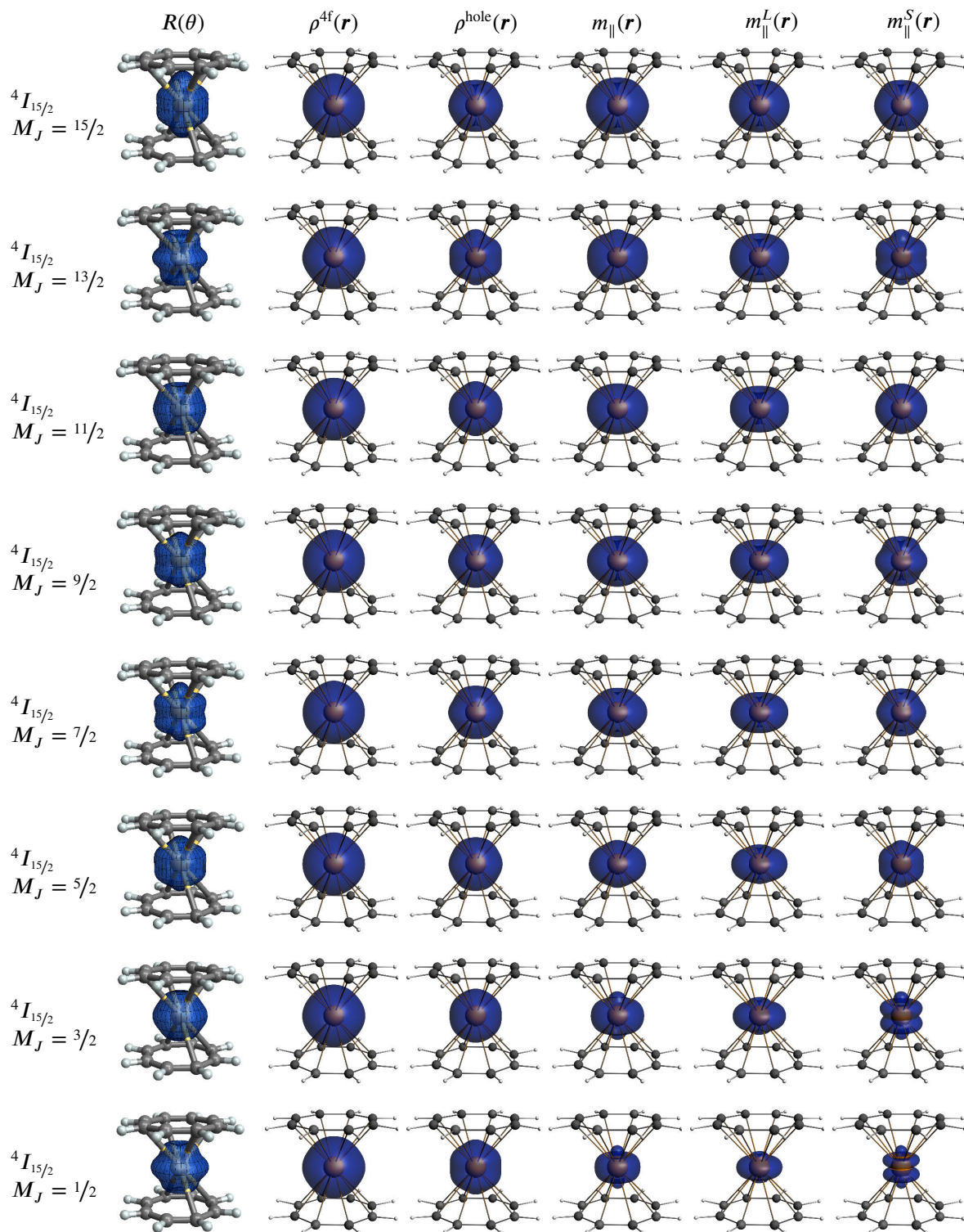


Figure 8: $\text{Er}(\text{COT})_2^-$: Angular dependence $R(\theta)$ of the 4f density according to Eq. 7,¹⁵ 4f electron density, and magnetizations for the magnetic axis \parallel . Isosurfaces at ± 0.001 au.

reasons as in $\text{Nd}(\text{COT})_2^-$, i.e. the lack of orbital angular momentum of the $4f_\sigma$ orbital along the \parallel direction, the orbital magnetization of the different M_J states is predominantly equatorially extended. The shape of the spin magnetization strongly differ both from the $R(\theta)$ function and from the electronic density $\rho^{4f}(\mathbf{r})$.

The shape of $m_{\parallel}^S(\mathbf{r})$ is easily interpreted with the help of the NSOs spin populations listed in Table 5. For instance, for $M_J = 15/2$ the contribution of the $4f_\sigma$ to the spin expectation value is zero which leads to an oblate spin magnetization. For comparison, the electron density of this M_J component has a prolate shape due to the spin-compensated doubly occupied $4f_\sigma$ NO. For partially occupied NOs, the relationship between the NO occupations and the NSO spin populations is not straightforward. In the $M_J = 1/2$ component, a major contribution to the spin magnetization arises from the $4f_\sigma$ NSO, causing its prolate appearance.

5 Conclusions and Outlook

Single-molecule magnetism is a topic of considerable interest in contemporary inorganic chemistry context, and theoretical support is critical in order to advance the field. Among the principal SMM design goals is a large magnetic anisotropy. The present analysis of the magnetic properties in the $\text{Ln}(\text{COT})_2^-$ series underlines the importance of the orbital angular momentum in the magnetic anisotropy of f -element complexes. For instance, the analysis of the orbital magnetization shows that equal occupations of $1/2$ or $3/2$ of pairs of the ‘textbook style’ real $4f$ orbitals with the same local symmetry π , δ , and in particular ϕ generate large orbital angular momentum contribution to the magnetization in the direction of a local symmetry axis around the metal center. The reason is that such occupations correspond to an electron or a hole for which the linear combination of real π , δ , or ϕ , orbitals represents a complex angular momentum eigenfunction with a complex Y_ℓ^m angular part. In the presence of the SO interaction, and/or when the local symmetry around the metal is only approximately axial, the orbital angular momentum is no longer a good quantum number but a theoretical analysis may still reveal a strong resemblance of the orbitals and their occupations to an idealized situation where L and S are good quantum numbers and maximally reinforce or cancel each other.

This work aims to highlight the availability of new theoretical tools, namely the generation of orbital and spin magnetizations, and natural orbitals and spin orbitals, at the SO multi-reference level of theory, for the investigation of the magnetic properties of f -element complexes. In combination with CF model wavefunctions, the visualization and analysis of the total magnetization and of its orbital and spin contribution, extracted from *ab-initio* wavefunctions, were performed on the $|J, M_J\rangle$ components of the GS of the entire $\text{Ln}(\text{COT})_2^-$ series, and were compared to the $4f$ charge density distributions of the Ln(III) ions. As emphasized previously by R&L,¹⁴ a ju-

icious choice of the metal ion and its environment is required in order to obtain a GS with a very large magnetic anisotropy. However, the limitations of a density-only based rationalization of the magnetic properties of f -element complexes are evidenced in the present study, suggesting that a detailed understanding of the contributions that lead to a given magnetic moment should be achieved with the help of *ab-initio* calculations.

For lanthanide-based complexes, a large magnetic anisotropy arises when the CF interactions splits the SO ground multiplet in such a way that the GS corresponds to the largest possible M_J components of the $^{2S+1}L_J$ GS term of the corresponding ion. In the second half of the lanthanide series this situation leads to particularly strong \parallel magnetic moments because the orbital and spin magnetizations reinforce each other with maximal values for M_L and M_S . The sandwich-type ligand geometry in the $\text{Ln}(\text{COT})_2^-$ series with its axial CF is well suited to maximize the anisotropy in the case of Pm, Sm, Gd, Er and Tm. Indeed, in agreement with the experimental data available, only in these cases the calculations produced a GS with the largest possible M_J . In these complexes, the combination of negative CF parameter B_2^0 and positive Stevens coefficient $\beta_J(2)$ leads to the largest \parallel magnetic moments. In terms of SMM behavior, these ions in an axial ligand field appear to be a good choice to generate very large magnetic anisotropy. On the contrary, the smallest M_J components was obtained for the GS of Ce and Tb due to the negative values of $\beta_J(2)$.

The graphical representations of $m_u^L(\mathbf{r})$ and $m_u^S(\mathbf{r})$, and the shapes of the natural orbitals representing the $4f$ density and corresponding spin orbitals, in combination with the calculated expectation values, are useful to analyze complicated wavefunctions in terms of chemically intuitive functions of 3D space and show the influence of the CF and SO coupling on the magnetic moment. The $4f$ electron density does not directly contain information about the magnetic moment, only indirectly via the underlying wavefunction. The analysis of the asphericities of the $4f$ electronic density and of the spin magnetizations has shown that the spin magnetization reflects the electron density in the first half of the series, whereas it represents the unpaired electrons in the second half of the series. This is in agreement with previous findings. However, the spin density may not be the main contributor to the $4f$ element magnetic moments. In the $\text{Ln}(\text{COT})_2^-$ series, the orbital moments are generally found larger in magnitude than the spin moments, and the orbital magnetization may strongly differ from the spin magnetization and warrants a separate analysis.

For truly complicated systems that are frequently encountered in SMM research, a careful analysis of *ab-initio* data has a great potential to guide the tuning of ligands once it is clear which orbitals are responsible for the observed magnetic moment and how spin and orbital angular momenta are balanced. A case in point, but focusing only on the spin magnetization because the orbital magnetization analysis was not available at the time, is a recent analysis of the magnetic exchange coupling in Lanthanide dimer complexes with very complicated electronic structures in

terms of NOs and NSOs.⁵⁷ An analysis of the orbital magnetization may prove to be similarly insightful in future applications. In follow-up work we plan to consider actinide complexes where the magnetizations should reveal participation of ligand orbitals due to the stronger covalent character of $5f$ vs. $4f$.

Acknowledgments

FG and JA acknowledge support from the U.S. Department of Energy, Office of Basic Energy Sciences, Heavy Element Chemistry program, under grant DE-SC0001136 (formerly DE-FG02-09ER16066). We acknowledge the Center for Computational Research (CCR) at the University at Buffalo for providing computational resources.

Supplementary Information

Additional technical information about the computations, energies and assignment of the electronic states at the SF and SO level of theory, details about the CF fit, plots of natural orbitals and natural spin orbitals for the ground states.

References

- [1] R. Sessoli, D. Gatteschi, A. Caneschi, M. A. Novak, *Nature*, 1993, **365**, 141–143.
- [2] R. J. Blagg, L. Ungur, F. Tuna, J. Speak, P. Comar, D. Collison, W. Wernsdorfer, E. J. L. McInnes, L. F. Chibotaru, R. E. P. Winpenny, *Nature Chem.*, 2013, **5**, 673–678.
- [3] L. Bogani, W. Wernsdorfer, *Nature Mat.*, 2008, **7**, 179–186.
- [4] R. A. Layfield, *Organometallics*, 2014, **33**, 1084–1099.
- [5] A. Cornia, M. Mannini, P. Sainctavit, R. Sessoli, *Chem. Soc. Rev.*, 2011, **40**, 3076–3091.
- [6] P. Zhang, L. Zhang, J. Tang, *Dalton Trans.*, 2015, **44**, 3923–3929.
- [7] J. Luzon, R. Sessoli, *Dalton Trans.*, 2012, **41**, 13556–13567.
- [8] N. Ishikawa, M. Sugita, T. Ishikawa, S.-Y. Koshihara, Y. Kaizu, *J. Am. Chem. Soc.*, 2003, **125**, 8694–8695.
- [9] N. Ishikawa, M. Sugita, W. Wernsdorfer, *Angew. Chem. Int. Ed.*, 2005, **44**, 2931–2935.

- [10] F. Pointillart, K. Bernot, S. Golhen, B. Le Guennic, T. Guizouarn, L. Ouhab, O. Cador, *Angew. Chem. Int. Ed.*, 2015, **54**, 1504–1507.
- [11] T. T. da Cunha, J. Jung, M.-E. Boulon, G. Campo, F. Pointillart, C. L. M. Pereira, B. Le Guennic, O. Cador, K. Bernot, F. Pineider, S. Golhen, L. Ouahab, *J. Am. Chem. Soc.*, 2013, **135**, 16332–16335.
- [12] D. N. Woodruff, R. E. P. Winpenny, R. A. Layfield, *Chem. Rev.*, 2013, **113**, 5110–5148.
- [13] R. Sessoli, A. K. Powell, *Coord. Chem. Rev.*, 2009, **253**, 2328–2341.
- [14] J. D. Rinehart, J. R. Long, *Chem. Sci.*, 2011, **2**, 2078.
- [15] J. Sievers, *Z. Phys. B - Condensed Matter*, 1982, **45**, 289–296.
- [16] N. F. Chilton, D. Collison, E. J. L. McInnes, R. E. P. Winpenny, A. Soncini, *Nature Communications*, 2013, **4**, 2551.
- [17] J. Baldoví, S. Cardona-Serra, J. M. Clemente-Juan, E. Coronado, A. Gaita-Ariño, *Chem. Sci.*, 2013, **4**, 938–946.
- [18] R. Skomski, D. J. Sellmyer, *Journal of Rare Earths*, 2009, **27**, 675–679.
- [19] D. Schimtt, *J. Phys.*, 1986, **47**, 677–681.
- [20] J. Boucherle, D. Givord, J. Schweizer, *J. Physique Colloq.*, 1982, **43**, C7–199.
- [21] K. Ayuel, P. F. de Châtel, *J. Magn. Magn. Mater.*, 2004, **277**, 43–59.
- [22] K. D. Warren, *Inorg. Chem.*, 1975, **14**, 3095–3103.
- [23] W. Liu, M. Dolg, P. Fulde, *Inorg. Chem.*, 1998, **37**, 1067–1072.
- [24] T. Kurikawa, Y. Negishi, F. Hayakawa, S. Nagao, K. Miyajima, A. Nakajima, K. Kaya, *J. Am. Chem. Soc.*, 1998, **120**, 11766–11772.
- [25] M. D. Walter, C. H. Booth, W. W. Lukens, R. A. Andersen, *Organomet.*, 2009, **28**, 698–707.
- [26] F. Ferraro, C. Aparecida Barboza, R. Arratia-Pérez, *J. Phys. Chem. A*, 2012, **116**, 4170–4175.
- [27] K. O. Hodgson, F. Mares, D. F. Starks, A. J. Streitwieser, *J. Am. Chem. Soc.*, 1973, **95**, 8650–8658.

- [28] M. Dolg, O. Mooßen, *J. Organomet. Chem.*, 2015, **794**, 17–22.
- [29] O. Mooßen, M. Dolg, *Chem. Phys. Lett.*, 2014, **594**, 47–50.
- [30] A. Kerridge, *Dalton Trans.*, 2013, **42**, 16428–16436.
- [31] A. Kerridge, R. Coates, N. Kaltsoyannis, *J. Phys. Chem. A*, 2009, **113**, 2896–2905.
- [32] M. Dolg, P. Fulde, H. Stoll, H. Preuss, A. Chang, R. M. Pitzer, *Chem. Phys.*, 1995, **195**, 71–82.
- [33] L. Ungur, L. F. Chibotaru, *Phys. Chem. Chem. Phys.*, 2011, **13**, 20086–20090.
- [34] S. K. Singh, T. Gupta, G. Rajaraman, *Inorg. Chem.*, 2014, **53**, 10835–10845.
- [35] J. J. Baldovi, S. Cardona-Serra, J. M. Clemente-Juan, E. Coronado, A. Gaita-Ariño, A. Palií, *Inorg. Chem.*, 2012, **51**, 12565–12574.
- [36] K. R. Meihaus, J. R. Long, *J. Am. Chem. Soc.*, 2013, **135**, 17952–17957.
- [37] L. Ungur, J. J. Le Roy, I. Korobkov, M. Murugesu, L. F. Chibotaru, *Angew. Chem.*, 2014, **126**, 1–6.
- [38] J. J. Le Roy, L. Ungur, I. Korobkov, L. F. Chibotaru, M. Murugesu, *J. Am. Chem. Soc.*, 2014, **136**, 8003–8010.
- [39] J. J. Le Roy, M. Jeletic, S. I. Gorelsky, I. Korobkov, L. Ungur, L. F. Chibotaru, M. Murugesu, *J. Am. Chem. Soc.*, 2013, **135**, 3502–3510.
- [40] J. J. Le Roy, I. Korobkov, J. E. Kim, E. J. Schelter, M. Murugesu, *Dalton Trans.*, 2014, **43**, 2737–2740.
- [41] F. Gendron, D. Pérez-Hernández, F.-P. Notter, B. Pritchard, H. Bolvin, J. Autschbach, *Chem. Eur. J.*, 2014, **20**, 7994–8011.
- [42] B. Pritchard, Ph.D. thesis, University at Buffalo, State University of New York, 2014.
- [43] A. Abragam, B. Bleaney, *Electron paramagnetic resonance of transition ions*, Clarendon Press, Oxford, 1970.
- [44] G. te Velde, F. M. Bickelhaupt, E. J. Baerends, S. J. A. van Gisbergen, C. Fonseca Guerra, J. G. Snijders, T. Ziegler, *J. Comput. Chem.*, 2001, **22**, 931–967.

- [45] C. Fonseca Guerra, J. G. Snijders, G. Te Velde, E. J. Baerends, *Theor. Chem. Acc.*, 1998, **99**, 391.
- [46] E. J. Baerends, T. Ziegler, J. Autschbach, D. Bashford, A. Bérces, F. M. Bickelhaupt, C. Bo, P. M. Boerrigter, L. Cavallo, D. P. Chong, L. Deng, R. M. Dickson, D. E. Ellis, M. van Faassen, L. Fan, T. H. Fischer, C. Fonseca Guerra, A. Ghysels, A. Giammona, S. J. A. van Gisbergen, A. W. Götz, J. A. Groeneveld, O. V. Gritsenko, M. Grüning, S. Gusarov, F. E. Harris, P. van den Hoek, C. R. Jacob, H. Jacobsen, L. Jensen, J. W. Kaminski, G. van Kessel, F. Kootstra, A. Kovalenko, M. V. Krykunov, E. van Lenthe, D. A. McCormack, A. Michalak, M. Mitoraj, J. Neugebauer, V. P. Nicu, L. Noodleman, V. P. Osinga, S. Patchkovskii, P. H. T. Philipsen, D. Post, C. C. Pye, W. Ravenek, J. I. Rodríguez, P. Ros, P. R. T. Schipper, G. Schreckenbach, J. S. Seldenthuis, M. Seth, J. G. Snijders, M. Solà, M. Swart, D. Swerhone, G. te Velde, P. Vernooijs, L. Versluis, L. Visscher, O. Visser, F. Wang, T. A. Wesolowski, E. M. van Wezenbeek, G. Wiesenekker, S. K. Wolff, T. K. Woo, A. L. Yakovlev, *Amsterdam Density Functional, SCM, Theoretical Chemistry, Vrije Universiteit, Amsterdam, The Netherlands.*, URL <http://www.scm.com>. Accessed 05/15. <http://www.scm.com>.
- [47] E. van Lenthe, E. J. Baerends, J. G. Snijders, *J. Chem. Phys.*, 1993, **99**, 4597–4610.
- [48] A. D. Becke, *J. Chem. Phys.*, 1993, **98**, 5648–5652.
- [49] E. J. Baerends, V. Branchadell, M. Sodupe, *Chem. Phys. Lett.*, 1997, **265**, 481–489.
- [50] F. Aquilante, L. De Vico, N. Ferré, G. Ghigo, P. Malmqvist, P. Neogrády, T. B. Pedersen, M. Pitoňák, M. Reiher, B. O. Roos, L. Serrano-Andrés, M. Urban, V. Veryazov, R. Lindh, *J. Comput. Chem.*, 2010, **31**, 224–247.
- [51] F. Gendron, B. Pritchard, H. Bolvin, J. Autschbach, *Inorg. Chem.*, 2014, **53**, 8577–8592.
- [52] A. Wolf, M. Reiher, B. A. Hess, *J. Chem. Phys.*, 2002, **117**, 9215–9226.
- [53] P.-A. Malmqvist, B. O. Roos, B. Schimmelpfennig, *Chem. Phys. Lett.*, 2002, **357**, 230–240.
- [54] S. K. Singh, T. Gupta, L. Ungur, G. Rajaraman, *Chem. Eur. J.*, 2015, **21**, 13812–13819.
- [55] H. Bolvin, *ChemPhysChem*, 2006, **7**, 1575–1589.
- [56] L. F. Chibotaru, L. Ungur, *J. Chem. Phys.*, 2012, **137**, 064112–22.
- [57] C. Y. Chow, H. Bolvin, V. E. Campbell, R. Guillot, J. W. Kampf, W. Wernsdorfer, F. Gendron, J. Autschbach, V. L. Pecoraro, , T. Mallah, *Chem. Sci.*, 2015, **6**, 4148–4159.

Table of Contents Graphics

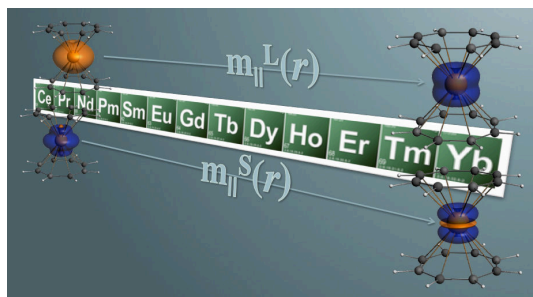


Table of Contents Synopsis

The orbital and spin magnetizations of the ground state of the $\text{Ln}(\text{COT})_2^-$ series are investigated at the *ab-initio* level.

